# Nanoscale Mapping of the Full Strain Tensor, Rotation, and Composition in Partially Relaxed $In_xGa_{1-x}N$ Layers by Scanning X-ray Diffraction Microscopy

Carsten Richter,[1,2,*] Vladimir M. Kaganer,[3] Armelle Even,[4,†] Amélie Dussaigne,[4] Pierre Ferret,[4] Frédéric Barbier,[4] Yves-Matthieu Le Vaillant,[5] and Tobias U. Schülli[2]

[1] *Leibniz-Institut für Kristallzüchtung (IKZ), Max-Born-Str. 2, Berlin 12489, Germany*
[2] *ESRF – The European Synchrotron, Grenoble Cedex BP 220, 38043, France*
[3] *Paul-Drude-Institut für Festkörperelektronik (PDI), Hausvogteiplatz 5–7, Berlin 10117, Germany*
[4] *University of Grenoble-Alpes, CEA, LETI, Minatec Campus, Grenoble F-38054, France*
[5] *Nelumbo Digital SAS, 143 rue du Brocey, Crolles 38920, France*

(Received 29 March 2022; revised 23 September 2022; accepted 6 October 2022; published 6 December 2022)

Strain and composition play a fundamental role in semiconductor physics, since they are means to tune the electronic and optical properties of a material and hence develop alternative devices. Today it is still a challenge to measure strain in epitaxial systems in a nondestructive manner, which becomes especially important in strain-engineered devices that often are subjected to intense stress. In this work, we demonstrate a microscopic mapping of the full tensors of strain and lattice orientation by means of scanning x-ray diffraction microscopy. We develop a formalism to extract all components of strain and orientation from a set of scanning diffraction measurements and apply the technique to a patterned $In_xGa_{1-x}N$ double layer to study strain relaxation and indium incorporation phenomena. The contributions due to varying indium content and threading dislocations are separated and analyzed.

DOI: 10.1103/PhysRevApplied.18.064015

## I. INTRODUCTION

Epitaxial thin films are the basis for most of modern semiconductor (opto)electronic devices, such as light-emitting diodes (LEDs), transistors, integrated circuits, etc. [1]. Lattice strain caused by a mismatch of lattice constants or thermal expansion coefficients between film and substrate is an important consequence of the growth, but also an opportunity to influence the electronic and optical properties of the material. Next to varying the alloy composition, strain engineering therefore is an established route to tune these properties.

Today, while transmission electron microscopy yields atomic resolution maps of lattice parameters [2,3], a nondestructive microscopic characterization of lattice strain with high accuracy is still not done routinely. Raman spectroscopy is used to study the impact of strain or alloy composition on phonon modes [4,5], allowing formulation of empirical models to indirectly relate strain to the measured Raman shift [6]. However, these are usually restricted to a certain component of the strain tensor and are limited to a range of known materials. Recent developments of scanning electron microscopy (SEM) techniques provide microscopic access to lattice deformations. High-resolution electron backscattered diffraction (EBSD) patterns analyzed by cross-correlation lead to an improved sensitivity to relative strain and rotation down to $10^{-4}$, which has been used to characterize local dislocation densities [7,8]. Electron channeling contrast imaging (ECCI) produces qualitative maps of lattice deformations with a high spatial resolution [9] that display individual dislocations and allow determination of their type even at high dislocation densities of $10^{10}$ $cm^{-2}$. A combination of these two techniques is used to determine the densities of screw, edge, and mixed dislocations in epitaxial InAlN films [10].

On the other hand, synchrotron-based x-ray diffraction microscopy techniques provide high lattice sensitivity and experienced an intensive development based on improved optics [11]. Focusing the beam now enables scanning x-ray diffraction microscopy (SXDM) measurements with a resolution down to tens of nanometers [12,13]. The use of a polychromatic ("white") beam leads to the simultaneous excitation of several Bragg reflections and the resulting Laue patterns provide information about the full strain tensor [14,15]. Furthermore, in the case of nano- and microparticles, the coherence of the synchrotron radiation and recent developments in phase retrieval allow for the lensless imaging of selected components of strain in three dimensions with a resolution below the beam size [16–18].

*carsten.richter@ikz-berlin.de
†Present address: OSRAM Opto Semiconductors GmbH, 93055 Regensburg, Germany.

 © 2022 American Physical Society

In this work, we focus on the development of SXDM to extract the full strain tensor, lattice orientation, and alloy composition in a semiconductor heterostructure. Compared to other techniques, SXDM stands out for being nondestructive, providing high lattice sensitivity below $10^{-5}$ of rotation and strain [12], access to buried layers and the compatibility with complex sample environments [19]. Today, the spatial resolution at state-of-the-art beamlines is in the several 10-nm range and SXDM gives direct, model-free information about the lattice parameters. Although the technique has already been applied to several material systems and devices to study strain and composition [20,21], former results were based on limited data and relied on assuming the crystallographic symmetry of the unstrained reference lattice. However, on the microscopic scale, no symmetry of the unit cell can be presumed because of an anisotropic local stress. This implies that all lattice parameters need to be refined in order to correctly decouple isotropic expansion of the lattice due to alloying and the anisotropic elastic strain as response to (local) stress. Hence, the knowledge of the full strain tensor is required, which also allows local dislocation densities to be inferred [10]. In x-ray diffraction (XRD), this means that the reciprocal space position of at least three noncoplanar Bragg reflections needs to be known for each real space position, as is demonstrated below.

We use the SXDM technique to study strain relaxation in an $In_xGa_{1-x}N$ (InGaN) heterostructure that serves as a template for the growth of multiple quantum well (MQW) structures. III-nitride semiconductors (GaN, InN, AlN, and their alloys) received huge attention and extensive development for their applications in electronics [22,23], particularly as light-emitting diodes (LEDs) [24,25] and power electronics [26]. The interest in the InGaN alloy is based on the potential of a direct electroluminescence at any wavelength of the visible spectrum [27] by tuning the In concentration. White-light emission is nowadays realized by indirect color conversion using phosphors excited with a short-wavelength nitride LED [28]. However, for future microdisplays with pixel size below 10 $\mu$m, a monolithic integration becomes advantageous. InGaN-based MQWs are the most promising candidates for this purpose but they still suffer from reduced efficiency at longer emission wavelengths due to limitations in the currently achievable In concentration of $< 30\%$ [29].

One approach for growing high-quality InGaN films with higher In content is to reduce the mismatch strain, which is a result of pseudomorphic growth on GaN substrates and the larger covalent radius of In compared to Ga. It has been shown for such strained films that a preference of In to occupy fourfold coordinated surface sites poses a limit to the indium concentration to 0.25 [30]. The large mismatch also results in mechanical stress at the interface and may result in additional defects like dislocations or V pits as the film thickness increases [31]. An obvious way to reduce the mismatch is to grow InGaN films on strain-relaxed InGaN buffer layers that have an in-plane lattice parameter close to the one of the functional InGaN film. An example for such a virtual substrate is InGaN on sapphire (InGaNOS) from Soitec [32,33], which is transferred from an initial InGaN/GaN donor structure using the Smart Cut$^{TM}$ technique [34]. After transfer, the InGaNOS seed layers are structured and annealed to facilitate strain relaxation and hence provide optimized in-plane lattice parameters for subsequent regrowth.

Here we demonstrate the capabilities of SXDM to map the full tensors of lattice strain and rotation, allowing investigation of the relaxation mechanisms in both layers of an InGaN/InGaNOS heterostructure. The results are discussed in the context of partial strain relaxation, variations of alloy composition, and strain fields around threading dislocations.

## II. EXPERIMENT

### A. Sample structure

Our sample is based on an InGaNOS pseudo substrate from Soitec with nominal in-plane lattice parameter of $a = 3.190$ Å corresponding to an In content of 3%, see Fig. 1. The (0001)-oriented InGaNOS is obtained through growth by metal-organic vapor phase epitaxy (MOVPE) of an InGaN seed layer on GaN and subsequent bonding of this layer onto a $SiO_2$-coated sapphire substrate. For strain relaxation, mesa structures with a side length of 800 $\mu$m are patterned by photolithography and dry etching, followed by several annealing steps. After the transfer and patterning, the InGaNOS seed-layer thickness is approximately 100 nm. Almost full relaxation of such mesa structures has been reported and they have successfully been used as a substrate for MQWs emitting in nearly the full visible range [31,32]. A second $In_xGa_{1-x}N$ layer of higher (nominally 5%) In content and a thickness of approximately 200 nm is grown on top of the InGaNOS pseudosubstrate by MOVPE. The relaxation of the InGaNOS reduces the lattice mismatch of the two layers and this way enables higher In uptake during epitaxy. Due to the patterning of the substrate, enhanced relaxation is to be expected at the edges of each pad. In this region, also a higher density of V pits can be seen in SEM images [see Fig. 3(a)].

### B. Scanning x-ray diffraction microscopy

SXDM measurements are carried out at beamline ID01 of the ESRF using a focused x-ray beam with submicron spot size and a fast, piezodriven scanning stage (see Fig. 2). Details of the setup have been described by Chahine *et al*. [12]. Continuous scans are performed unidirectionally by driving the piezostage at constant speed during synchronized readout of the area detector (MaxiPix 4)

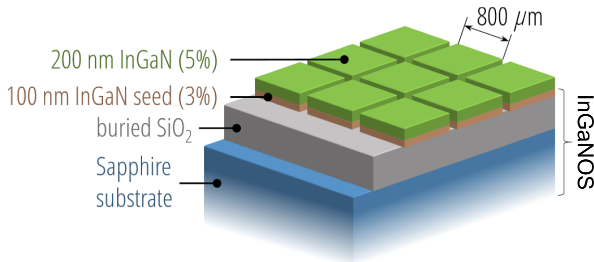


FIG. 1. Sketch of the sample (not drawn to scale). An InGaN seed layer with nominal In content of 3% (orange) has been bonded onto $SiO_2$-coated sapphire. After patterning and heat treatment, a layer with the In content of 5% (green) is epitaxially grown on top of the thus obtained InGaNOS virtual substrate.

[35] at a frame rate of 100 $s^{-1}$. The detector samples a two-dimensional (2D) region of reciprocal (angular) space defined by its pixel size (55 $\mu$m), the number of pixels (516 × 516), its distance to the sample (approximately 670 mm) and the x-ray energy (see below). By subsequently changing the angle of beam incidence $\eta$, a three-dimensional (3D) reciprocal space map (RSM) $I(i,j,\eta)$ is probed. Here $(i,j)$ are the row and column of the detector, respectively. Based on a calibration of the detector position and orientation, we convert these data to Cartesian coordinates of reciprocal space $I(Q_x,Q_y,Q_z)$. This is done for all points $(x,y)$ on the sample surface resulting in a five-dimensional (5D) intensity distribution $I(x,y,Q_x,Q_y,Q_z)$. Before this conversion, a drift correction is usually needed in order to compensate the parasitic motion of the sample on changing the incidence angle, which is due to limitations in the alignment and the rigidity of the setup. The

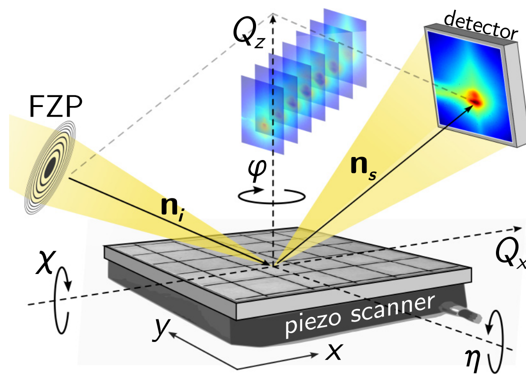


FIG. 2. Illustration of the SXDM setup with definition of the coordinate system. The beam is focused [e.g., by a Fresnel zone plate (FZP)] onto the sample. While the sample is scanned through the beam, the detector continuously records images of diffracted intensity. Each frame corresponds to a 2D slice of the 3D reciprocal space $\mathbf{Q}$, which is defined by the direction of incident and scattered beam and the x-ray wavelength $\lambda$: $\mathbf{Q} = 2\pi/\lambda\,(\mathbf{n}_s - \mathbf{n}_i)$. By rocking about the $\eta$ axis, a 3D volume of reciprocal space is probed.

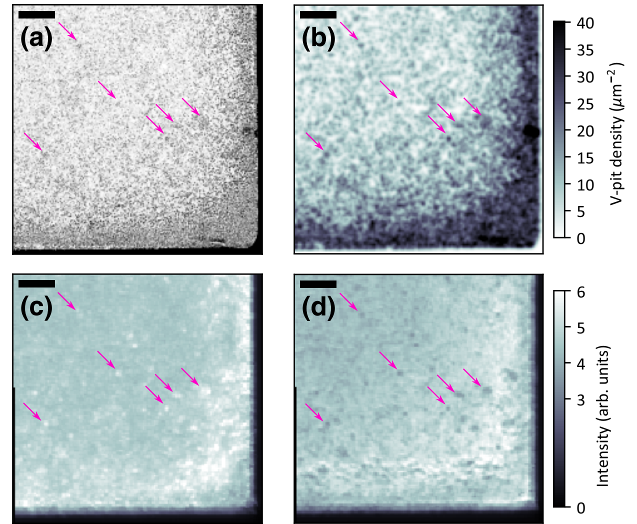


FIG. 3. SEM of the studied corner region (a) compared to integrated intensity from SXDM of the InGaNOS seed layer (c) and the overgrown InGaN layer (d). The dark dots in (a) are V pits in the InGaN film. Subfigure (b) shows the V-pit density, which has been approximated based on the SEM image. One can see from (b),(d) that clusters of V pits result in a minimum of diffracted intensity. The arrows point at some clusters of V pits that are seen in all datasets. The scale bars correspond to 5 $\mu$m.

drift is typically in the range below 1 $\mu$m/deg. The criterion we use to assess the amount of drift is to minimize the variance of the spatial distribution of integrated intensity, which is increased by any drift of the sample. The correction is then performed by subpixel shifting the maps $I_{i,j,\eta}(x,y)$ for each set of $i,j,\eta$.

We use a Cartesian reciprocal coordinate frame $\mathbf{Q}$ that is fixed to the sample (see Fig. 2). The surface normal of the (0001)-oriented InGaN/InGaNOS sample is chosen as $Q_z$ direction, which corresponds to the vertical direction when all diffractometer angles are zero. $Q_x$ is chosen to be along the in-plane direction $[10\bar{1}0]$, which leads to $Q_y \parallel [\bar{1}2\bar{1}0]$. We acquire 5D SXDM data sets in coplanar geometry for three different Bragg reflections, the symmetric 0004 reflection and the asymmetric pair $10\bar{1}3$ and $0\bar{1}13$, to provide sensitivity to all lattice parameters. For each of them, we measure the same sample area of 40 × 40 $\mu m^2$ at a corner of a partially relaxed mesa structure with a resolution of 150 × 150 points resulting in a step size of 267 nm in both directions. Figures 3(c) and 3(d) show the average intensity (integrated over reciprocal space $Q_x,Q_y,Q_z$) obtained for this region next to the corresponding SEM image.

The diffracted intensity and the SEM image show similar features. For easier comparison, the SEM image [Fig. 3(a)] has been resampled [Fig. 3(b)] to match the resolution of the x-ray measurement [Figs. 3(c) and 3(d)]. This way, Fig. 3(b) approximately illustrates the density of V pits as gray scale. Comparing this to the x-ray images

of the two layers, one can see that a high V-pit density results in a reduced diffraction intensity for the top layer [Fig. 3(d)]. This is expected since a V pit means a loss of diffracting volume. In contrast, a slight increase of intensity from the InGaNOS seed layer is observed [Fig. 3(c)]. We explain this by a strongly inhomogeneous In distribution within the volume probed by the x-ray nanobeam near V pits. In general, our peak fit routine allows separation of the Bragg peak from both layers even for regions with a large number of V pits (see Fig. S5 within the Supplemental Material for small distances to the mesa edge [36]). However, near V pits, a small part of the probed volume of the top layer may have a strongly reduced In content, which then would lead to an enhanced diffraction into the region of reciprocal space associated with the InGaNOS seed layer. While the peak position is not affected by minor parts of the probed volume showing strong deviations from the average, the intensity will reflect this change of scattering volume. Below, we describe the effect of the In content and how to determine it from SXDM measurements in detail.

SXDM measurements of symmetric and asymmetric reflections are carried out during two different experimental sessions and therefore under slightly different beam conditions. The symmetric reflection is measured using x rays with energy of 8 keV focused by a Fresnel zone plate (FZP) down to $(h, v) \approx (130, 90)$ nm in horizontal and vertical direction, respectively. On the other hand, for the asymmetric reflections the energy is tuned to 7 keV providing the possibility to have almost normal incidence of x rays and, hence, a smaller footprint and higher spatial resolution. For the latter case, a Kirkpatrick-Baez mirror system is used for focusing down to $(h, v) \approx (150, 200)$ nm. Overall, the beam footprint is 200 nm or below, which is smaller than the scan step size.

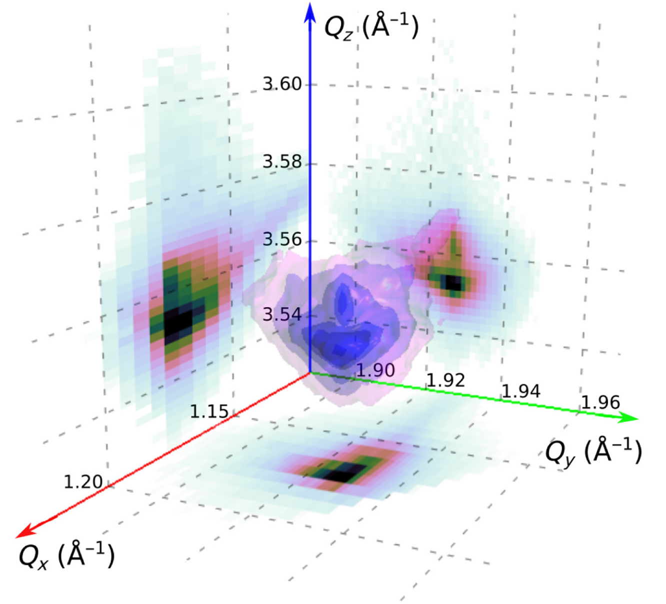


FIG. 4. Intensity distribution in 3D RSM in vicinity of the $0\bar{1}13$ reflection for a single spot on the sample and projections along the Cartesian axes $Q_z \parallel 0001$ (blue), $Q_x \parallel 10\bar{1}0$ (red), and $Q_y$ (green). The spacing of intensity isosurfaces corresponds to a factor of three in intensity.

## III. RESULTS AND DISCUSSION

### A. Reciprocal space maps

Figure 4 shows one of the collected 3D RSMs and its projections along the principle Cartesian axes as an example for the $0\bar{1}13$ reflection. The data shows some typical features expressed in many parts of the sample. Two distinct maxima at different $Q_z$ positions correspond to the two pseudomorphic InGaN layers: the InGaNOS virtual substrate (at higher $Q_z$) and the top InGaN layer (stronger peak at lower $Q_z$). Streaks in the angular directions (rotation about $Q_x$ and $Q_y$) are due to local lattice tilt. The main goal of the data reduction is to extract the center position of both peaks from each of the (in total 67 500) 3D RSMs.

The local lattice deformations are studied in terms of the orientation and strain state of the crystallographic unit cells. The intensity distribution in reciprocal space is related to the strain and tilt distribution of the unit cells averaged over the probed volume. In our case, it is defined by the beam footprint and the layer thickness and is on the order of $\approx 150 \times 200 \times 150$ nm$^3$. Furthermore, we analyze only the average lattice properties in such a volume element, which is derived from the peak position (e.g., center of mass of intensity) in reciprocal space $\mathbf{Q}_c = (\overline{Q_x}, \overline{Q_y}, \overline{Q_z})$. Representing $\mathbf{Q}_c$ in spherical coordinates, one directly obtains the interplanar spacing $d$ of the diffracting lattice planes from the radial component $d = 2\pi/|\mathbf{Q}_c|$, whereas the angular components contain contributions from both tilt and strain. Due to the similar lattice parameters of the two investigated InGaN layers, we had to fit two strongly overlapping peaks (see Fig. 4 and Fig. S5 within the Supplemental Material [36]) to determine positions of both peaks. For each RSM, we perform a double-peak fit on radial projections $(I(x, y, |\mathbf{Q}|)$, since these provided the clearest peak separation. For both of the two resulting peak positions along $|\mathbf{Q}|$, we calculate the centers of mass for the two other (angular) projections and convert the results back to Cartesian coordinates. Thus, we reduce the 5D dataset $I(x, y, Q_x, Q_y, Q_z)$ to vector fields of the type $\mathbf{Q}_c(x, y)$ for each of the three measured reflections. In order to combine the $\mathbf{Q}_c$ data of the three noncoplanar Bragg reflections (which allows tilt and strain to be disentangled) one needs to match the surface coordinates $(x, y)$ of all data sets. This is achieved by correlating the angular components of $\mathbf{Q}_c$ that carry a contribution of the local lattice tilt for all reflections.

### B. Derivation of local lattice parameters and orientation

The general equation relating the measured momentum transfer **Q** of a certain reflection *hkl* with the crystal orientation and lattice parameters is [37]

$$\begin{pmatrix} Q_x \\ Q_y \\ Q_z \end{pmatrix} = \mathbf{U}(\varphi, \chi, \eta) \cdot \mathbf{B}(a, b, c, \alpha, \beta, \gamma) \cdot \begin{pmatrix} h \\ k \\ l \end{pmatrix}. \tag{1}$$

Assuming that the crystallographic symmetry is locally fully broken by strain (space group *1*), the matrix **B** depends on all six lattice parameters $(a, b, c, \alpha, \beta, \gamma)$ while the matrix **U** takes account of the local orientation of the probed crystalline volume, e.g., in terms rotation about the three Cartesian axes $(\chi, \eta, \varphi$, see Fig. 2). Thus, the system of Eq. (1) containing nine unknowns becomes determined with the data collected for at least three noncoplanar reflections.

In practice, relative variations in the components of $\mathbf{Q}_c$ can be determined very precisely. However, the accuracy of absolute values is limited and leads to offsets in the resulting lattice parameters. This is mainly due to the sphere of confusion of the diffractometer, its limited stiffness, but also the fact that we remounted the sample for one of the measurements. It is critical to correct the average offsets of $\mathbf{Q}_c$ by using a reference, for example, based on reflections of a known substrate or by comparing the sample average of $\mathbf{Q}_c$ to lab-based, integrating XRD measurements. We use the latter approach and tune the offsets of the diffractometer angles such that the Bragg peak positions from lab XRD agree with those determined by SXDM after integrating over the sample. Here, we also assume that, on average across the sample, the hexagonal symmetry of the unit cells holds. With these boundary conditions, we could correct the $(\overline{Q_x}, \overline{Q_y}, \overline{Q_z})$ values and determine the average orientation matrix **U**. Subsequently, local variations of orientation and lattice parameters can be determined by solving Eq. (1) for each point on the sample and for both InGaN layers. Local orientation is described by applying an additional rotation matrix $\Delta\mathbf{U}(\Delta\varphi, \Delta\chi, \Delta\eta)$, whereas lattice strain is treated by refining the components of **B**.

A more straightforward procedure can be formulated for a given set of three noncoplanar reflections. In our case, based on the reciprocal lattice vectors $\mathbf{Q}_{0004}$, $\mathbf{Q}_{10\bar{1}3}$, and $\mathbf{Q}_{0\bar{1}13}$, we can calculate the basis vectors of the reciprocal lattice, $\mathbf{b}_1, \mathbf{b}_2$, and $\mathbf{b}_3$, via

$$\begin{aligned} \mathbf{b}_3 &= \mathbf{Q}_{0004}/4, \\ \mathbf{b}_1 &= \mathbf{Q}_{10\bar{1}3} - 3\mathbf{b}_3, \\ \mathbf{b}_2 &= -(\mathbf{Q}_{0\bar{1}13} - 3\mathbf{b}_3). \end{aligned}$$

The real-space basis vectors are then commonly obtained via $\mathbf{a}_i = 2\pi V \mathbf{b}_j \times \mathbf{b}_k$ with $V$ being the unit cell volume and $(i, j, k) = (1, 2, 3)$ and its cyclic permutations. From these vectors, the six lattice parameters can be readily calculated by all combinations of their scalar products, which represent the metric tensor. They are shown for the top InGaN layer in Fig. 5.

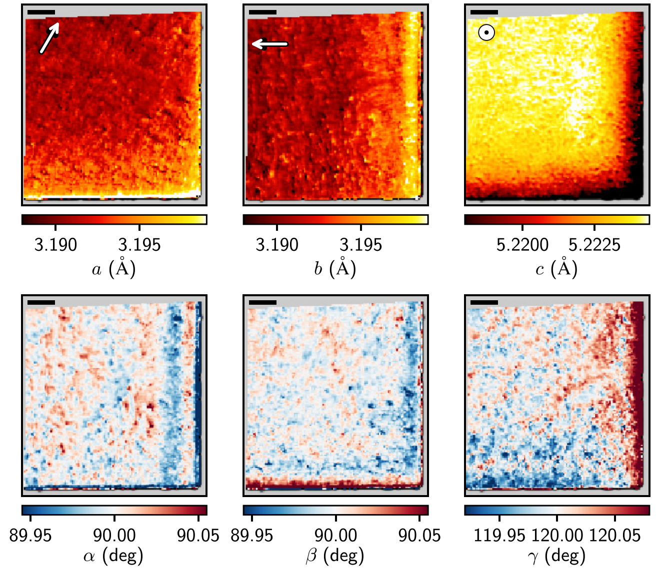


FIG. 5. Maps of all lattice parameters for the top InGaN layer. Arrows indicate the directions of the lattice basis vectors. Gray areas indicate missing data at the border regions due to a limited scan range either in real or reciprocal space for at least one of the three measured reflections. The scale bars correspond to 5 $\mu$m.

Now, in order to derive rotation and strain of the lattice, we need to define a reference unit cell $(\mathbf{a}_1^0, \mathbf{a}_2^0, \mathbf{a}_3^0)$ based, for instance, on the sample average or on that of a reference compound (here, GaN) or substrate. At any surface position, the measured unit cell (averaged over the beam footprint) is then a linear transformation **T** of the reference

$$\mathbf{a}_i = T_{ij}\,\mathbf{a}_j^0. \tag{2}$$

Thus, we can obtain the transformation matrix $T_{ij}$ by writing the local basis vectors in matrix form and using the inverse of the reference system:

$$\mathbf{T} = (\mathbf{a}_1, \mathbf{a}_2, \mathbf{a}_3)\left(\mathbf{a}_1^0, \mathbf{a}_2^0, \mathbf{a}_3^0\right)^{-1}. \tag{3}$$

From this transformation matrix, we can moreover compute the local rotation and strain tensors by means of *polar decomposition* into an orthogonal rotation matrix **U** and a symmetric matrix **P** such that **T** = **UP**. The matrix **P** then relates to the total strain $f_{ij}$ via

$$P_{ij} = \delta_{ij} + f_{ij}, \tag{4}$$

where $\delta_{ij}$ is the Kronecker delta. The rotation matrix **U** can in general be factored into three matrices describing the

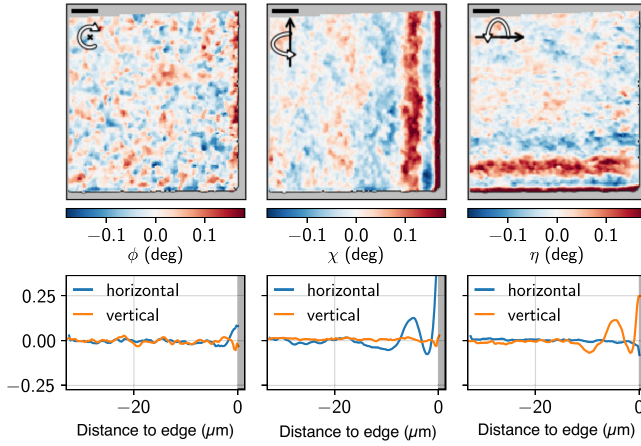


FIG. 6. Rotation components $\Delta\varphi$ (yaw, $\omega_{xy}$), $\Delta\chi$ (roll, $\omega_{yz}$), and $\Delta\eta$ (pitch, $\omega_{xz}$) for the top InGaN layer. The bottom row shows projections along both sample axes. Strong tilts can be seen at the edges of the sample, which is connected to a decaying waviness towards the center of the pad. Gray areas indicate missing data at the border regions due to a limited scan range either in real or reciprocal space. The scale bars correspond to 5 $\mu$m.

rotation about any axes of the Cartesian system and thus be converted into Eulerian angles [38]. However, in most cases, the changes in lattice orientation are very small and can be described by infinitesimal rotation that has negligible effect on the other rotation axes. In that case, the local lattice rotation $\omega_{ij}$ is obtained via

$$U_{ij} = \delta_{ij} + \omega_{ij}, \tag{5}$$

where $\Delta\phi = \omega_{xy}$, $\Delta\chi = \omega_{yz}$, and $\Delta\eta = \omega_{zx}$.

Figure 6 illustrates the obtained orientational variation of the crystal lattice in terms of these three angles. Here, we show only results for the regrown top InGaN layer, because maps of the two layers are almost identical and hardly any differences are visible by the eye (see Fig. S3 within the Supplemental Material [36]). According to the RSM ranges, we can detect tilts up to approximately 1°. It can be seen that the lattice is strongly tilted outwards near the edges related to the relaxation of strain. This is followed by a decaying undulation when going towards the center of the pad. The angle $\varphi$ corresponds to the twist of unit cells and does not show this undulation but also increases towards the edges of the mesa.

### C. Separating elastic strain and alloy composition

The components of the total strain $f_{ij}$ consist of two contributions. The change of indium concentration in a volume element gives rise to its homogeneous expansion, provided this volume element is not restricted by the surrounding material. The respective strain $\varepsilon^*_{ij}$, called eigenstrain or intrinsic strain, is not connected to stress by itself. Yet, an inhomogeneous eigenstrain causes stress, and hence elastic strain $\varepsilon_{ij}$, since the neighboring volume elements restrict each other. Other lattice defects, particularly dislocations, also contribute to the elastic strain and stress. Thus, the total strain **f** can be presented by the sum

$$f_{ij} = \varepsilon^*_{ij} + \varepsilon_{ij} \tag{6}$$

of the eigenstrain $\boldsymbol{\varepsilon}^*$ due to the indium concentration variation and the elastic strain $\boldsymbol{\varepsilon}$ that gives rise to stress $\boldsymbol{\sigma}$ via Hooke's law:

$$\sigma_{ij} = C_{ijkl}\varepsilon_{kl}, \tag{7}$$

where $C_{ijkl}$ is the elastic stiffness tensor. Both $\boldsymbol{\sigma}$ and $\boldsymbol{\varepsilon}$ are symmetric rank-2 tensors. Their diagonal and off-diagonal components represent normal and shear stress and strain, respectively. In the wurtzite structure of InGaN, the stiffness tensor has only five independent components and its symmetry is such that there is no cross-talk between shear and normal strain [39]. We assume that this symmetry is maintained for small deformations of the unit cells.

The surface of the film is free from applied forces and hence $\sigma_{zz} = 0$ at the surface. If the variation of the indium concentration over the depth can be neglected, the condition $\sigma_{zz} = 0$ is satisfied also in the bulk of the film (plane-stress approximation). Via Hooke's law, this condition allows disentanglement of elastic and eigenstrain and hence yields a map of the indium concentration in the film. For (0001)-grown epitaxial layers with wurtzite structure, Eq. (7) becomes [39]

$$\sigma_{zz} = 0 = C_{13}\varepsilon_{xx} + C_{13}\varepsilon_{yy} + C_{33}\varepsilon_{zz}, \tag{8}$$

where the Voigt notation is used and the symmetry of the stiffness tensor gives $C_{13} = C_{23}$. We note that, on microscopic level, the in-plane isotropy $\varepsilon_{xx} = \varepsilon_{yy}$ cannot be assumed. After rearranging Eq. (8), $C_{13}/C_{33}$ remains as the only unknown parameter, which can be substituted by $\nu/(1-\nu)$ with $\nu$ being the material-dependent Poisson ratio. For a given indium content $x_{\mathrm{In}}$ in $\mathrm{In}_x\mathrm{Ga}_{1-x}\mathrm{N}$, $\nu(x_{\mathrm{In}})$ and the relaxed lattice parameters are derived by linear interpolation of values known for the binary compounds InN and GaN. The reference lattice parameters $\mathbf{a}^0_i$ and hence the eigenstrain $\varepsilon^*_{ij}$ are defined with respect to GaN:

$$\nu(x_{\mathrm{In}}) = x_{\mathrm{In}}\nu_{\mathrm{InN}} + (1 - x_{\mathrm{In}})\nu_{\mathrm{GaN}}, \tag{9}$$

$$\varepsilon^*_{xx}(x_{\mathrm{In}}) = \varepsilon^*_{yy}(x_{\mathrm{In}}) = x_{\mathrm{In}}\left(\frac{a_{\mathrm{InN}}}{a_{\mathrm{GaN}}} - 1\right), \tag{10}$$

$$\varepsilon^*_{zz}(x_{\mathrm{In}}) = x_{\mathrm{In}}\left(\frac{c_{\mathrm{InN}}}{c_{\mathrm{GaN}}} - 1\right), \tag{11}$$

$$\varepsilon^*_{ij} = 0,\ i \neq j.$$

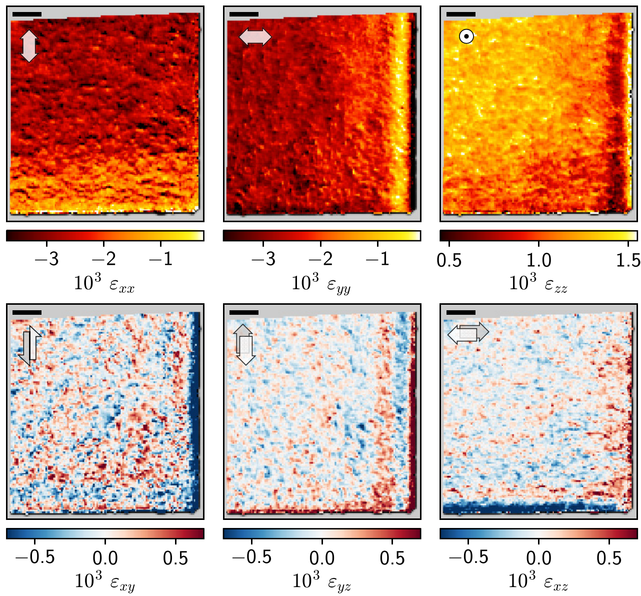


FIG. 7. The normal (top row) and shear (bottom row) components of elastic strain for the InGaNOS seed layer. Directions of strains are indicated by arrows. Scale bars correspond to 5 $\mu$m.

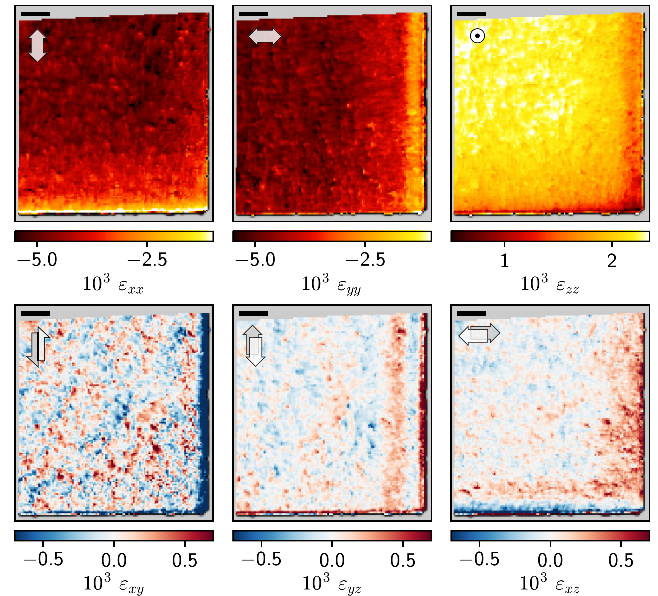


FIG. 8. The normal (top row) and shear (bottom row) components of elastic strain for the regrown InGaN top layer. Directions of strains are indicated by arrows. Scale bars correspond to 5 $\mu$m.

We use the following values from Ref. [40]: $a_{\mathrm{GaN}} = 3.1878$ Å, $c_{\mathrm{GaN}} = 5.185$ Å, $a_{\mathrm{InN}} = 3.538$ Å, $c_{\mathrm{InN}} = 5.703$ Å, $\nu_{\mathrm{GaN}} = 0.183$, $\nu_{\mathrm{InN}} = 0.272$.

Given the expression for total strain $f_{ij}$ in Eqs. (6) and (9)–(11), the plane-stress condition Eq. (8) results in an equation that is quadratic in $x_{\mathrm{In}}$ as the only unknown. It can be solved analytically and has only one root in the range $0 < x_{\mathrm{In}} < 1$. The solution for every surface coordinate $(x, y)$ provides spatial maps of strain and alloy composition of the layer. The former are shown in Figs. 7 and 8 for the top InGaN layer and the InGaNOS seed layer, respectively. The composition maps for both layers are shown in Fig. 9.

The maps in Figs. 6–9 reveal strong changes of the lattice orientation, strain, and In content at the mesa edges (the right and the bottom edges of the maps). The in-plane strain components $\varepsilon_{xx}$ and $\varepsilon_{yy}$ in Figs. 7 and 8 relax each at the edge where the respective strain component is normal to the edge (i.e., $\varepsilon_{xx}$ relaxes at the bottom edge while $\varepsilon_{yy}$ relaxes at the right edge), which is expected due to an absence of geometrical restrictions. For the InGaNOS pseudo substrate (Fig. 7), nearly full strain relaxation is observed for the corresponding components. As a consequence of relaxation, the out-of-plane strain $\varepsilon_{zz}$ reduces at both edges. As mentioned before, this is linked to lattice undulations setting at a 10 $\mu$m away from the edge (see Fig. 6). The spacial frequency of the undulations increases as the edge of the mesa is approached. Note that the maps of lattice rotation are nearly identical for both InGaN layers (see Fig. S3 within the Supplemental Material [36]). It is not yet clear how strain relaxation leads to this buckling effect.

In Fig. 9(b), one can see a reduced In uptake in the regrown InGaN layer close to the edges of the mesa structure, which stands in contrast to what is expected based on the relief of compressive strain in these regions. A comparison to Fig. 3(a) shows that this loss of In is connected to an increased V-pit density. Such a reduced In concentration near V pits has already been observed before [21]. It may be the result of a disturbed growth such as changes in the relative diffusion length of In and Ga due to the high defect density. As expected, the In distribution in the InGaNOS seed layer is hardly affected, since it was formed before the patterning took place.

The derivation of the composition maps is based on the plane-stress approximation in Eq. (8). While $\sigma_{zz} = 0$ is satisfied at the sample surface, the average through the film may be nonzero due to a depth dependence of the composition or due to defects (dislocations, V pits, etc.) that result in a three-dimensional distribution of strain. The plane-stress approximation further implies that all three components of the stress tensor $\sigma_{iz}$ are equal to zero. Due to the symmetry of the stiffness tensor for the wurtzite structure, this would result in $\varepsilon_{xz} = \varepsilon_{yz} = 0$. Therefore, the corresponding experimental maps allow the plane-stress approximation and the consistency of the composition analysis to be cross-checked.

We estimate the local deviation of the hexagonal symmetry of the stiffness tensor due to local lattice rotation and find that these are more than an order of magnitude too small to have a noticeable effect. Our experimental data in

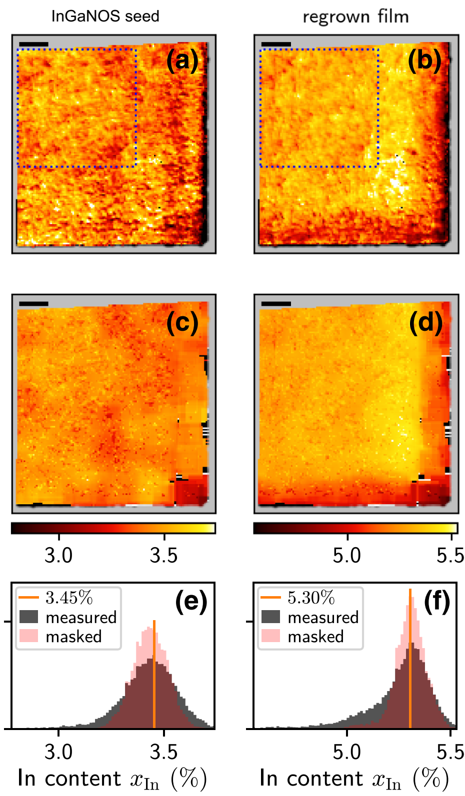


FIG. 9. Top: maps of the indium content $x_{\mathrm{In}}$ in both layers: InGaNOS seed (a) and the regrown InGaN layer (b). The same maps after excluding regions with shear strain $|\varepsilon_{xz}| > 10^{-4}$ or $|\varepsilon_{yz}| > 10^{-4}$ are shown in (c),(d). These masked out regions have been filled by interpolation from remaining data points. The corresponding histograms are shown in (e),(f). Scale bars correspond to 5 $\mu$m. The 20 × 20 $\mu$m$^2$ area far away from edges, which is used for statistical analysis below is marked by a dotted blue line in (a),(b).

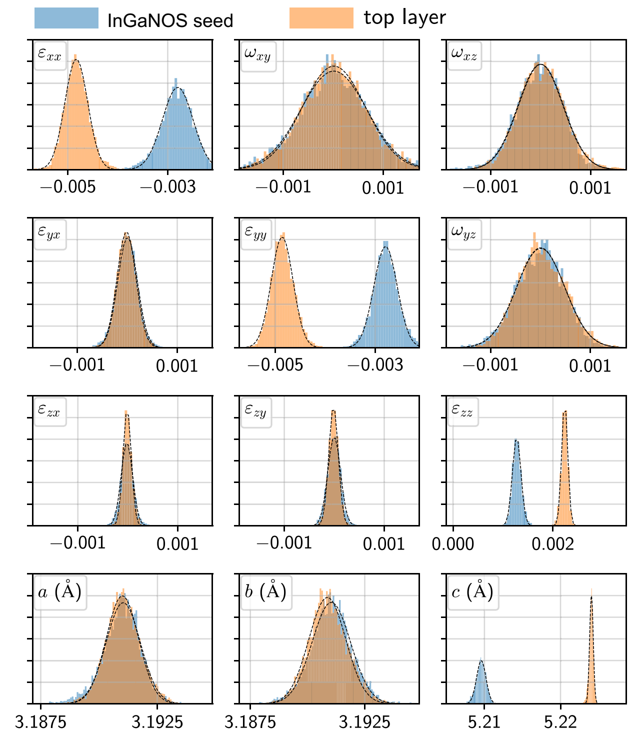


FIG. 10. Histograms of elastic strain and lattice rotation in both InGaN layers derived from the maps in Figs. 6–8. For the histograms of strain and rotation, the same ranges are used for the abscissae to facilitate the comparison. Gaussian fits are shown by dashed lines and the mean values and standard deviations are presented in Table I.

Figs. 7 and 8 show regions with comparably small, but still significant variations of $\varepsilon_{xz}$ and $\varepsilon_{yz}$, which is also reflected in the histograms in Fig. 10. We can use these maps to exclude regions where the plane-stress approximation is violated or where experimental error is high. For this purpose, we isolate the part of the maps where $|\varepsilon_{xz}| < 10^{-4}$ and $|\varepsilon_{yz}| < 10^{-4}$ keeping approximately a third of all data points. This results in a much narrower distribution of the In content [see Figs. 9(e) and 9(f)]. We then interpolated the data from valid data points to fill the remaining regions and obtain a much smoother spatial distribution [see Figs. 9(c) an 9(d)] where the short-range (approximately 1 $\mu$m) variations of In content nearly disappear. One should note that the interpolation would lead to a smoother impression of the maps in any case. The histograms in Figs. 9(e) and 9(f) are more meaningful: they show that in the regions of small out-of-plane shear strain, the In-concentration variations are also small. Still, for the regrown top InGaN layer, an obvious decrease of In content at the mesa edges remains. Within the region with less than 5 $\mu$m distance from the edge, a total number of valid points of 500 remains. Even though this is a rather small number, it is statistically relevant and all valid measurements in this region show a trend towards a reduced In content of the top layer of 5%. As discussed above, this fits into the overall picture, since the top layer exhibits a large number of V-pit defects as a side effect of layer transfer and patterning. We also note that a deviation from the plane-stress approximation gives an error to the calculated In content $x_{\mathrm{In}}$ that mostly affects the results for the out-of-plane strain $\varepsilon_{zz}$. This can be exemplary seen by comparing total strain and elastic strain in Fig. 11.

In Sec. S4 within the Supplemental Material [36], we furthermore simulate the three-dimensional strain fields of threading dislocations as another source of error for the composition maps. We generate a spatial distribution of dislocations that is characteristic for our case (see Sec. III F below) and perform the same analysis as was done with the measured strain maps according to Eq. (8). This provides an estimate of the error that can be introduced by dislocations into the determination of In content (see Fig. S4 within the Supplemental Material [36]). In our case, this error turns out to be minor.

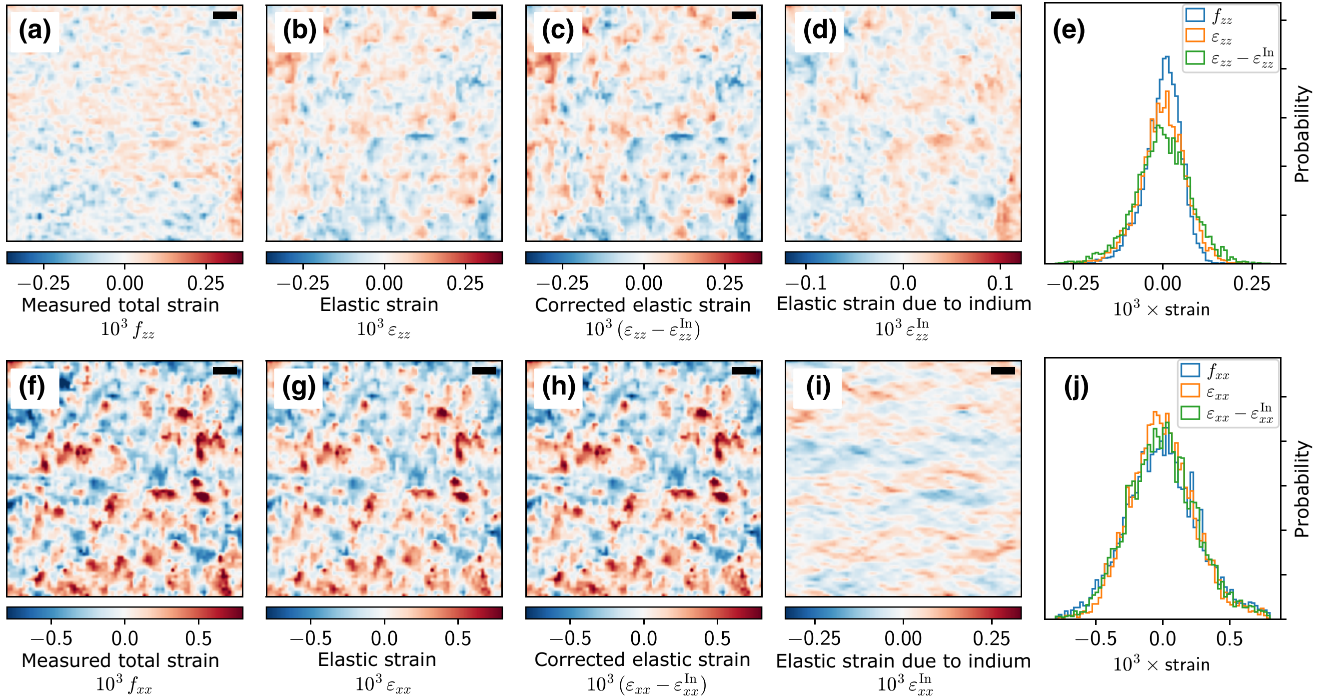


FIG. 11. (a) Total strain $f_{zz}$ as measured by x-ray diffraction, (b) elastic strain $\varepsilon_{zz}$ after subtraction of the eigenstrain $\varepsilon^*$, (c) corrected elastic strain $\varepsilon_{zz} - \varepsilon_{zz}^{\mathrm{In}}$ after subtracting the elastic strain $\varepsilon_{zz}^{\mathrm{In}}$ (d) that is due to inhomogeneous In concentration, (e) histograms of the $zz$ components of total, elastic, and corrected strain. (f)–(j) the same data as (a)–(e) for the $xx$ component of the strain tensors. The size of all maps is $20 \times 20\ \mu\mathrm{m}^2$.

### D. Statistical comparison of lattice parameters

In the following sections, we focus our analysis on a $20 \times 20\ \mu\mathrm{m}^2$ region in the bulk part of the mesa, where the edge effects are not essential [marked as dotted squares in the top-left corners of the maps Figs. 9(a) and 9(b)]. We first consider the statistical characteristics of the maps and then discuss possible origins of the variations in terms of the microstructure.

Figure 10 shows the histograms obtained from the maps of strain, rotation, and lattice parameters for both bottom and top layer. The variations of lattice rotations $\omega_{ij}$ are larger, and shear strain is smaller compared to the normal strain components. The narrower In distribution of the top InGaN film [see Fig. 9(d)] relates to the narrower distribution of the out-of-plane lattice parameter $c$. The histograms of the in-plane lattice parameters $a$ and $b$ of the two layers coincide, since the layers are epitaxially linked. The distributions of the normal strains in the plane therefore reflect the variations of the indium content. The histograms can be well described by normal distributions as shown in Fig. 10 by dotted lines. Their mean values and standard deviations are presented in Table I.

One can see by eye that the maps of strain components (Figs. 7 and 8) exhibit sharper features compared to the maps of rotation (Fig. 6), which is not reflected in the histograms. To quantify this effect, it is useful to look at autocorrelation functions of the respective maps. The autocorrelations for the top InGaN layer are shown in Fig. 12. The other autocorrelation functions for both layers are presented in Figs. S1 and S2 within the Supplemental Material [36]. We define a characteristic length scale as a distance where the radial correlation function (after azimuthal integration) drops to half of its maximum value. These lengths are given in Table I next to the other statistical parameters. One should keep in mind, that the experimental resolution of approximately 200 to 300 nm poses a lower boundary to the autocorrelation lengths.

In general, we can see variations on the micrometer scale in all of the experimental maps, which has been observed in $\mathrm{In}_x\mathrm{Ga}_{1-x}\mathrm{N}$ films before [21,41]. It also appears that the lattice parameters, strains and rotations of the top InGaN layer vary on longer length scales compared to the seed layer. That may be a result of the averaging over a twice larger layer thickness leading to increased lateral averaging due to an inclination of the x-ray beam with respect to the layer plane. The only clear exception is the out-of-plane lattice parameter $c$. The data in Table I also reveals the significantly (approximately twice) larger autocorrelation lengths for the rotation components in comparison to the strain components. The lattice rotation is usually related to threading dislocations of edge or screw type in epitaxial GaN layers [40]. The high degree of correlation of

TABLE I. Statistical parameters of the virtual substrate (InGaNOS) and the regrown InGaN layer. Only a $20 \times 20\ \mu m^2$ sample area omitting the edges of the mesa (top-left corner) is taken into account [marked by dotted squares in Figs. 9(a) and 9(b)]. The autocorrelation lengths are defined as the distance where the radial autocorrelation function drops to half of its value at zero distance (see Figs. S1 and S2 within the Supplemental Material [36]). The Pearson $r$ value characterizes the cross-correlation between the InGaNOS seed and top InGaN layer.

| Quantity | Mean value ± standard deviation | | Autocorrelation length (nm) | | Cross-correlation |
|---|---|---|---|---|---|
| (unit) | InGaNOS seed | Top layer | InGaNOS seed | Top layer | Pearson $r$ |
| $\alpha$ (deg) | $90 \pm 0.014$ | $90 \pm 0.011$ | 722 | 895 | 0.61 |
| $\beta$ (deg) | $90 \pm 0.013$ | $90 \pm 0.009$ | 635 | 750 | 0.56 |
| $\gamma$ (deg) | $120 \pm 0.020$ | $120 \pm 0.019$ | 651 | 711 | 0.55 |
| $a$ (Å) | $3.1910 \pm 0.0007$ | $3.1910 \pm 0.0007$ | 587 | 667 | 0.56 |
| $b$ (Å) | $3.1909 \pm 0.0009$ | $3.1908 \pm 0.0008$ | 741 | 859 | 0.64 |
| $c$ (Å) | $5.2096 \pm 0.0006$ | $5.2241 \pm 0.0002$ | 974 | 609 | 0.09 |
| $\omega_{xy} = \Delta\varphi$ (mrad) | $0.01 \pm 0.60$ | $-0.01 \pm 0.63$ | 1104 | 1169 | 0.96 |
| $\omega_{yz} = \Delta\chi$ (mrad) | $0.00 \pm 0.48$ | $-0.01 \pm 0.48$ | 1460 | 1428 | 0.96 |
| $\omega_{zx} = \Delta\eta$ (mrad) | $0.00 \pm 0.45$ | $-0.01 \pm 0.45$ | 1395 | 1512 | 0.92 |
| $x$ (%) | $3.459 \pm 0.098$ | $5.305 \pm 0.063$ | 805 | 862 | 0.56 |
| $\varepsilon_{xx}$ ($10^{-3}$) | $-2.80 \pm 0.31$ | $-4.83 \pm 0.22$ | 711 | 758 | 0.39 |
| $\varepsilon_{yy}$ ($10^{-3}$) | $-2.79 \pm 0.23$ | $-4.86 \pm 0.22$ | 744 | 837 | 0.61 |
| $\varepsilon_{zz}$ ($10^{-3}$) | $1.28 \pm 0.08$ | $2.24 \pm 0.06$ | 766 | 751 | 0.33 |
| $\varepsilon_{xy}$ ($10^{-3}$) | $0.01 \pm 0.19$ | $0.02 \pm 0.19$ | 648 | 731 | 0.62 |
| $\varepsilon_{xz}$ ($10^{-3}$) | $0.02 \pm 0.11$ | $0.01 \pm 0.08$ | 646 | 798 | 0.62 |
| $\varepsilon_{yz}$ ($10^{-3}$) | $0.01 \pm 0.13$ | $0.01 \pm 0.09$ | 722 | 895 | 0.61 |

the maps of rotation components in top and bottom layers thus show that the dislocations are mostly inherited from the virtual substrate.

While the distributions of rotations with the in-plane rotation axes (tilt, $\omega_{xz}$ and $\omega_{yz}$) have nearly identical values of both width and correlation length, they significantly differ from rotations about the surface normal (twist, $\omega_{xy}$). This fits well into the picture of threading dislocations, since threading edge ($a$-type) dislocations contribute to the twist while threading screw ($c$-type) dislocations contribute to the tilt components [42,43]. A quantitative analysis of the strain distributions and the autocorrelation functions is presented in Sec. III F below. In a simplified picture according to Ref. [44] for randomly distributed dislocations, taking the standard deviations of the rotation parameters in Table I, we obtain densities of $1.2 \times 10^8\ cm^{-2}$ and $5.1 \times 10^8\ cm^{-2}$ for screw and edge dislocations, respectively. Since we assume normal distributions (see Fig. 10), we introduce a factor of $\sqrt{2\pi}$ to convert the standard deviation into the integral breadth. Comparing with Fig. 3(b), we can see that the V-pit density is on the same order of magnitude in the considered upper-left corner of the sample.

### E. Elastic strain due to laterally inhomogeneous indium composition

An inhomogeneous distribution of In in the film gives rise to elastic strain. The aim of this section is to evaluate this strain and subtract it from the strain measured by x-ray diffraction. The difference is attributed to threading dislocations and considered in the next section.

A homogeneous In distribution in GaN results in a homogeneous lattice expansion, similar to thermal expansion. Moreover, since the relative changes of $a$ and $c$ lattice parameters between GaN and InN are almost identical (approximately 10%), the strain due to a homogeneous indium concentration $x_{\mathrm{In}}$ is isotropic: $\varepsilon^*_{ij} = \varepsilon^* \delta_{ij}$ and $\varepsilon^* = x_{\mathrm{In}} \Delta a/a$. This strain (eigenstrain or intrinsic strain, in terminology of the theory of internal stresses) is equivalent to a thermal strain $\varepsilon^* = \alpha \Delta T$, where $\alpha$ is thermal expansion coefficient and $\Delta T$ temperature difference. The strain $\varepsilon^*$ describes a homogeneous crystal expansion, which itself does not cause elastic strain and stress, provided that a piece of material with the strain $\varepsilon^*$ is not constrained by the surrounding material.

The constraints imposed by the continuity of the material for an inhomogeneous indium distribution, i.e., for $\varepsilon^*(\mathbf{r})$ varying in space, give rise to an additional elastic strain, which can be found by solving the elastic equilibrium equations. The solution of the respective thermoelastic problem for the strain due to an inhomogeneous temperature distribution in a thin plate is well known [45]. Hexagonal symmetry of GaN in (0001) plane gives rise to the transverse elastic isotropy, so that the isotropic solution can be used with the Poisson ratio $\nu_h = C_{12}/(C_{11} + C_{12})$ (using Voigt notation). For the elastic moduli of GaN [46],

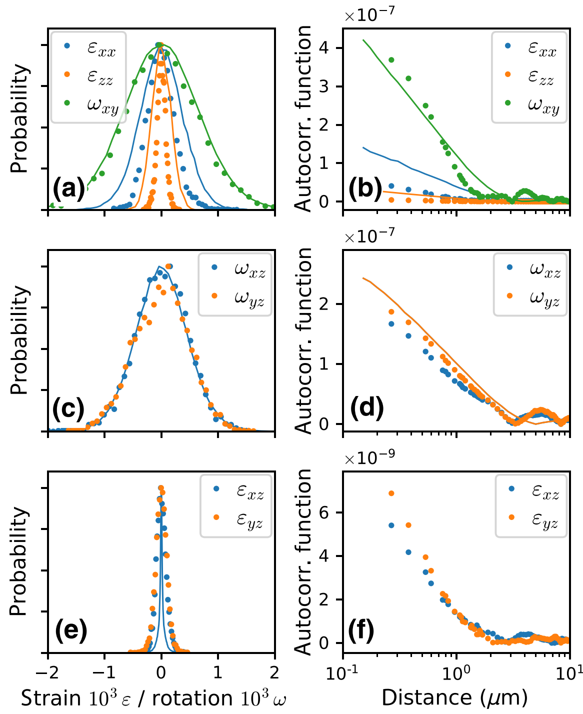


FIG. 12. Comparison of histograms and autocorrelation functions of the measured and simulated distributions of strain $\varepsilon_{ij}$ and rotation $\omega_{ij}$. (a),(b) The in-plane strain and rotation components, as well as the normal strain $\varepsilon_{zz}$, that are attributed to edge threading dislocations with the density of $2 \times 10^9$ cm$^{-2}$. (c),(d) The tilt components $\omega_{xz}, \omega_{yz}$ attributed to screw threading dislocations with the density of $4 \times 10^8$ cm$^{-2}$. The dislocations are modeled by random dislocation pairs with the Wilkens' parameters $M = 10$ for edge and $M = 7$ for screw dislocations to optimize the correlation lengths. The distances between dislocations in the pairs are described by a lognormal distribution with a standard deviation set to half of the mean distance between dislocations in the pairs. (e),(f) The shear strain components $\varepsilon_{xz}, \varepsilon_{yz}$ that are expected to be zero in the plane-stress approximation. Note that the scale in (f) is different from that in (b),(d). The measured data are shown by circles, whereas Monte Carlo simulations for edge and screw dislocations are shown by lines.

we get $\nu_h \approx 0.27$. Hence, it remains to reformulate the thermoelastic solution in our notation.

The solution [45] is expressed through the thermoelastic potential $\Psi$ satisfying the equation

$$\frac{\partial^2 \Psi}{\partial x^2} + \frac{\partial^2 \Psi}{\partial y^2} = (1 + \nu_h)\varepsilon^*(x, y). \tag{12}$$

The displacements are $u_x = \partial\Psi/\partial x$, $u_y = \partial\Psi/\partial y$, and the components of the elastic strain due to an inhomogeneous In distribution $\varepsilon_{ij}^{\text{In}} = \frac{1}{2}(\partial u_i/\partial x_j + \partial u_j/\partial x_i)$ are

$$\varepsilon_{xx}^{\text{In}} = \frac{\partial^2 \Psi}{\partial x^2},\ \varepsilon_{yy}^{\text{In}} = \frac{\partial^2 \Psi}{\partial y^2},\ \varepsilon_{xy}^{\text{In}} = \frac{\partial^2 \Psi}{\partial x \partial y},\ \varepsilon_{zz}^{\text{In}} = (1 + \nu_h)\varepsilon^*. \tag{13}$$

The average of the eigenstrain $\varepsilon^*(x, y)$ over the plate produces a homogeneous expansion and can be subtracted. Hence, we consider in Eq. (12) the eigenstrain with zero average value. The effect of the borders of the plate is restricted, according to Saint-Venant's principle, to a stripe of the width comparable with the characteristic length of the fluctuations in the In concentration. Since our area of interest is well away from the borders, we neglect the boundary conditions to Eq. (12) and solve it by Fourier transformation of the eigenstrain

$$\varepsilon^*(\mathbf{r}) = \int \varepsilon_{\mathbf{k}}^* e^{-2\pi i \mathbf{k}\cdot\mathbf{r}} d\mathbf{k}, \tag{14}$$

where $\mathbf{r}$ and $\mathbf{k}$ are the two-dimensional radius vector and wave vector, respectively. Solving Eq. (12) and substituting the solution in Eq. (13), we get for the in-plane components of the strain due to an inhomogeneous In distribution in a thin plate

$$\varepsilon_{ij}^{\text{In}}(\mathbf{r}) = (1 + \nu_h) \int \frac{k_i k_j}{k^2} \varepsilon_{\mathbf{k}}^* e^{-2\pi i \mathbf{k}\cdot\mathbf{r}} d\mathbf{k} \quad (i, j = 1, 2). \tag{15}$$

The $\varepsilon_{zz}^{\text{In}}$ component is calculated directly by the last expression in Eq. (13).

We show below that the $f_{zz}$ component of total strain as measured by x-ray diffraction contains a substantial contribution due to the inhomogeneous In distribution, while the effect of In on the in-plane strain components is minor. Hence, we begin the analysis with the $\varepsilon_{zz}^{\text{In}}$ component. Figure 11(a) is the map $f_{zz}$ for the top layer, measured by x-ray diffraction (the average over the map is subtracted). Figure 11(b) shows the elastic strain $\varepsilon_{zz}$, which is the difference between the total strain $f_{zz}$ and the eigenstrain $\varepsilon^*$ obtained from the In concentration map $x_{\text{In}}$ [see Fig. 9(b)]. We subtract the elastic strain due to inhomogeneous indium concentration $\varepsilon_{zz}^{\text{In}}$, which is calculated by Eq. (13) and shown in Fig. 11(d). The remaining elastic strain is shown for comparison in Fig. 11(c). Figure 11(e) compares the probability distributions of the measured total strain $f_{zz}$, the derived elastic strain $\varepsilon_{zz}$, and the remaining elastic strain after subtracting the elastic strain $\varepsilon_{zz}^{\text{In}}$ due to an inhomogeneous In distribution. This latter quantity is attributed to threading dislocations and is discussed below.

Figures 11(f)–11(i) show the same data for the in-plane components of strain $f_{xx}$ and $\varepsilon_{xx}$. One can see that, in this case, the correction is negligible. This is confirmed by the histograms in Fig. 11(j) of the probability distributions of the prior and after the correction to the strain due to In. The effect on the other in-plane strain components $\varepsilon_{xy}$ and $\varepsilon_{yy}$ is also negligible compared with the accuracy of the measurements. Hence, the measured maps of the in-plane strain components are due to the strain from sources different from the In distribution.

### F. Elastic strain due to threading dislocations

We attribute the remaining strain in the film to threading dislocations crossing the film along its normal. For the present density of dislocations, the resolution of the measurements is not sufficient to resolve individual threading dislocations. However, it is possible to analyze the linear superpositions of their strain and rotation fields, which are a result of the measurement. In Sec. S1 of the Supplemental Material [36], we derive explicit formulas for all components of the strain and rotation tensors due to dislocations crossing the film along its normal, taking account of the elastic stress relaxation on the free surfaces of the film. These fields consist of two contributions: the long range ($\propto \rho^{-1}$) field provides the main contribution to the probability distributions and the correlation functions described below, while further relaxation terms decay faster with the distance $\rho$ from the dislocation line and give rise to only a little correction of the results. The long-range parts of the strain components are directly related to the dislocation strains and rotations in an infinite medium.

An edge dislocation in an infinite medium gives rise to strain in the plane perpendicular to the dislocation line. When a thin film is cut perpendicular to the dislocation line, the components of the strain at distances $\rho$ exceeding the film thickness are

$$\varepsilon_{\rho\rho} = \varepsilon_{\phi\phi} = -\frac{b_x}{4\pi}(1-\nu_h)\frac{\sin\phi}{\rho},$$
$$\varepsilon_{\rho\phi} = \frac{b_x}{4\pi}(1+\nu_h)\frac{\cos\phi}{\rho},\ \varepsilon_{zz} = \nu_h\frac{b_x}{2\pi}\frac{\sin\phi}{\rho}, \tag{16}$$

where $b_x$ is the Burgers vector. Here we describe the components in cylindrical coordinates (see in Sec. S1 of the Supplemental Material [36]). The in-plane strain components in the film differ from the respective expressions for the dislocation strain in the infinite medium by a substitution of the Poisson ratio $\nu_h$ with $\nu_h/(1+\nu_h)$ (the plane-stress solution). The strain $\varepsilon_{zz}$ arises to provide zero normal stress, $\sigma_{zz} \propto (1-\nu_h)\varepsilon_{zz} + \nu_h(\varepsilon_{\rho\rho} + \varepsilon_{\phi\phi}) = 0$. The strains $\varepsilon_{\rho z}$ and $\varepsilon_{\phi z}$ are zero in the infinite medium and decay faster than $\rho^{-1}$ in the film. The in-plane rotation due to an edge dislocation is the same as in the infinite medium,

$$\omega_{\rho\phi} = \frac{b_x}{2\pi}\frac{\cos\phi}{\rho}, \tag{17}$$

while $\omega_{\rho z}$ and $\omega_{\phi z}$ decay faster than $\rho^{-1}$.

The displacement field of a screw dislocation in an infinite medium $u_z = (b_z/2\pi)\phi$, where $b_z$ is the Burgers vector, gives rise to the strain and rotation $\varepsilon_{\phi z} = \omega_{\phi z} = b_z/4\pi\rho$. In a thin film, the long-range strain $\varepsilon_{\phi z}$ is zero to provide a stress-free boundary condition. As a result, the rotation in the film

$$\omega_{\phi z} = \frac{b_z}{2\pi\rho} \tag{18}$$

is 2 times larger than it is in the infinite medium, and remains the only long-range component of the strain and rotation tensors; all other components decay faster than $\rho^{-1}$. The corrections to the strain and rotation tensors at the distances from the dislocation line comparable with the film thickness are derived in Sec. S1 of the Supplemental Material [36] and provide only small corrections to the strain and rotation fields.

Threading dislocations in GaN are correlated, to reduce elastic energy due to their slowly decaying strain fields [47]. These correlations can be modeled by pairs of dislocations with opposite Burgers vectors. When the mean distance $R$ between dislocations in the pairs exceeds the distance between dislocations in the crystal $r_d = 1/\sqrt{\varrho}$, where $\varrho$ is the density of threading dislocations (i.e., the density of the pairs is $\varrho/2$), the pairs overlap [48]. The range of the correlations can be described by the dimensionless parameter $M = R/r_d = R\sqrt{\varrho}$, introduced by Wilkens [49–51]. In his model of the "restrictedly random dislocation distribution," the crystal is divided in cells, each cell containing $M$ dislocations with the total Burgers vector equal to zero. Modeling by dislocation pairs, with the parameter $M$ defining the mean distance between dislocations in the pair, is more convenient and gives very close diffraction profiles [48]. Further details of the Monte Carlo modeling of the dislocation arrays are given in Appendix A.

We adjust the parameters $\varrho$ and $M$ for both threading screw and threading edge dislocations so that the histograms and autocorrelations obtained from Monte Carlo modeling of the strain and rotation fields agree with the experiment. We primarily fit the rotation components, since they are larger than strains. The in-plane rotation $\omega_{xy}$, as well as the in-plane strain components $\varepsilon_{xx}, \varepsilon_{xy}, \varepsilon_{yy}$ and the strain normal to the plane $\varepsilon_{zz}$, are attributed to edge dislocations and presented in Figs. 12(a) and 12(b). The tilt components $\omega_{xz}$ and $\omega_{yz}$ are attributed to screw dislocations and presented in Figs. 12(c) and 12(d). The obtained densities of screw and edge dislocations are $4\times10^{8}$ cm$^{-2}$ and $2\times10^{9}$ cm$^{-2}$ , respectively, about 4 times larger than those obtained above (see Sec. III D) following Ref. [44]. The correlation parameters are found to be $M = 10$ for edge and $M = 7$ for screw dislocations. Hence, the respective distances of the screening of the strain fields of dislocations by surrounding dislocations $R = M/\sqrt{\varrho}$ are 2.2 and 3.5 $\mu$m for edge and screw dislocations. These screening distances are directly seen in Figs. 12(b) and 12(d) as the intersections of the straight lines (in the lin-log scale) with the ordinate axis.

The shear strain components $\varepsilon_{xz}$ and $\varepsilon_{yz}$ [Figs. 12(e) and 12(f)] are zero in the plane-stress approximation. The Monte Carlo calculation in Fig. 12(e) is performed using three-dimensional strain fields of the dislocations in the film derived in Sec. S1 of the Supplemental Material [36]. Both edge and screw dislocations with the densities and correlations obtained above are included in the calculation. One can see from Figs. 14(a) and 14(c) in Appendix A, that at equal densities, screw dislocations provide larger contribution to $\varepsilon_{xz}$ and $\varepsilon_{xz}$ compared to edge dislocations. As a result, screw dislocations with smaller density and edge dislocations with larger density give comparable contributions to the curve.

The observed variations of $\varepsilon_{xz}$ and $\varepsilon_{yz}$ in the experimental histograms in Fig. 12(e) are larger than the simulated ones, but remain significantly smaller than those of the other strain or rotation components. They can be attributed either to experimental error or to limitations of the model. Particularly, we did not consider potential variations of the indium content over the depth and the residual stress on the film due to the bonding on the handling wafer.

## IV. CONCLUSIONS

The present work demonstrates that scanning x-ray diffraction microscopy can be used to obtain quantitative maps of all six lattice parameters and of the local orientation of the unit cells in an epitaxial thin film. We present a general formalism for an unambiguous transfer of the SXDM data of at least three Bragg reflections into microscopic maps of the total strain and the lattice rotation. We use the technique to map strain and rotation in a patterned InGaN/InGaN double layer with different indium concentrations bonded to a handling wafer. The maps reveal variations of strain and orientation on the micrometer scale as well as partial relaxation that involves a buckling at the edge of the patterned mesa structures.

We discuss potential contributions to the obtained maps and quantified specifically the effect of a varying indium concentration as well as the strain and rotation fields due to edge and screw threading dislocations. This way, we extract maps of indium content for both (i.e., top and bottom) layers of the structure and characterized the distribution of threading dislocations, although the individual dislocations are not resolved in the experiment. As pointed out in Appendix A, resolving individual dislocations may be achieved with an x-ray beam spot size that is approximately 5 times smaller than in our experiment, which is available at dedicated synchrotron beamlines.

We find that, in the bulk part of the mesa, the dislocations in the top layer are inherited from the bottom layer, so that regrowth with a higher indium concentration does not result in a nucleation of additional dislocations. However, the layer transfer and patterning processes lead to an increased amount of defects and V pits at the mesa edge. The data shows that this results in a reduced indium incorporation into the top layer that is grown after the patterning. Therefore, the increased relaxation and the thus reduced compressive tensile strain at the edge seems to be less relevant for the indium concentration than the disturbed growth close to defects.

We discuss the limitations of the technique and the analysis of composition. The range of variations in $\varepsilon_{xz}$ and $\varepsilon_{xz}$ provides an estimate of the limited experimental accuracy as well as the applicability of the plane-stress condition $\sigma_{iz} = 0$ $(i = x, y, z)$ on the microscopic scale. Finally, our work paves the way for a more routine application SXDM to study the strain distribution in epitaxial layers, microstructures and devices with the potential to probe buried layers or samples in a complex environment.

## ACKNOWLEDGMENTS

We acknowledge the ESRF for beamtime at beamline ID01, the Institut de Recherche Technologique (IRT) NanoElectronique for supporting the use of the ESRF, and Soitec for the furniture of the InGaNOS wafer and for their support. V.M.K. thanks Alexander Belov (Institute of Crystallography, Moscow) for useful discussions. C.R. thanks Michael Hanke (PDI) for estimating shear stresses based on a depth inhomogeneity of the In concentration.

## APPENDIX A: PROBABILITY DISTRIBUTIONS AND CORRELATION FUNCTIONS OF THE STRAIN AND ROTATION COMPONENTS FOR DISLOCATION ARRAYS

In this Appendix, we describe the Monte Carlo modeling of the dislocation arrays. Figure 13(a) shows the strain $\varepsilon_{xx}$ due to a dislocation pair consisting of two edge dislocations with the opposite Burgers vectors. Here and below, all calculations are made for a free-standing film of thickness $2l = 300$ nm, and the strain components are averaged over the interval $0 < z < l$. Figure 13(b) presents the strain $\varepsilon_{xx}$ due to such pairs of edge dislocations uniformly distributed with the dislocation density $\varrho = 1\ \mu\mathrm{m}^{-2}$ and $M = 8$. The direction of the vector between the two dislocations of a pair is random, the Burgers vectors possess one of three orientations 120° with respect to each other. Since $M$ is larger than 1, the strain fields of the pairs overlap and the individual pairs cannot be recognized in the map. We take a lognormal distribution of the distances between dislocations in a pair, with the mean distance $R = M/\sqrt{\varrho}$. The standard deviation of this distribution is set to $R/2$.

Figure 13(c) shows the same map as in Fig. 13(b) but with a 5 times worse resolution, obtained by averaging the strain over the pixel size of 0.265 $\mu$m, representing the resolution of the experiment. The individual dislocations cannot be revealed anymore. However, the strain distribution is only a little affected. Figure 13(d) compares the strain probability distributions obtained from the maps

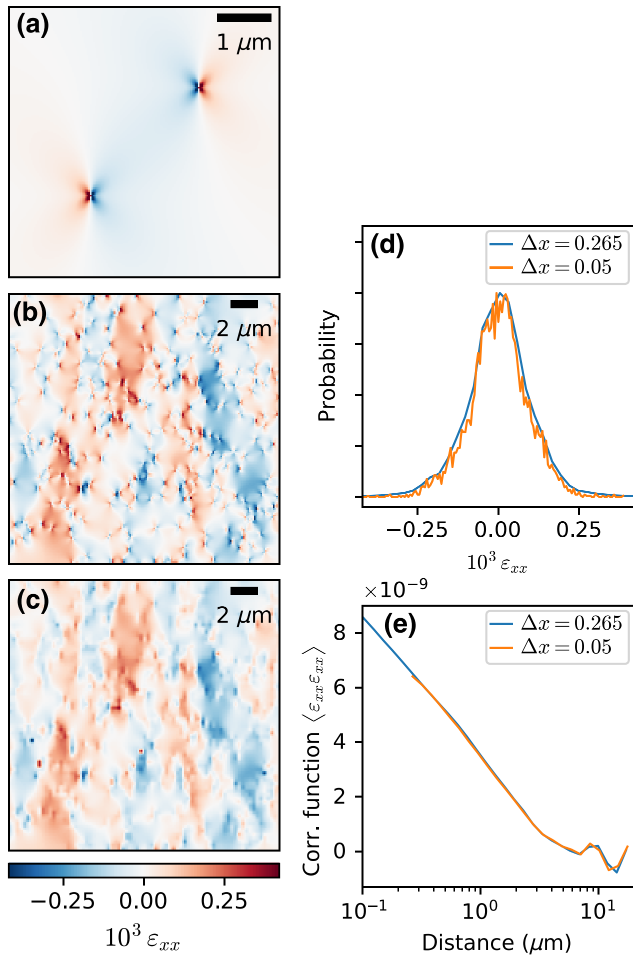


FIG. 13. (a) Strain $\varepsilon_{xx}$ due to a pair of edge dislocations with the opposite Burgers vectors, (b) a $20 \times 20\ \mu\text{m}^2$ map of the strain $\varepsilon_{xx}$ due to such dislocation pairs randomly and uniformly distributed with the dislocation density $\varrho = 1\ \mu\text{m}^{-2}$ and $M = 8$, the pixel size is 0.05 $\mu$m, (c) the same map for a pixel size of 0.265 $\mu$m, (d) the strain probability densities, and (e) the autocorrelation functions obtained from the two maps. The size of the maps is $20 \times 20\ \mu\text{m}^2$.

in Figs. 13(b) and 13(c). The strain distribution is only smoothed out at a lower resolution of the map. Figure 13(e) presents the autocorrelation function of the strain in the maps, considered below in detail. Here, we note only that the resolution has very little effect on the correlation function as well.

The dimensions of the maps presented in Figs. 13(b) and 13(c) correspond to these of the experimental maps. As a result, the probability distribution in Fig. 13(d) and the autocorrelation function in Fig. 13(e) possess limited statistics. Monte Carlo modeling allows us to improve statistics by repeating the calculation many times and averaging the results. Such averaged quantities are presented in Figs. 14 and 15.

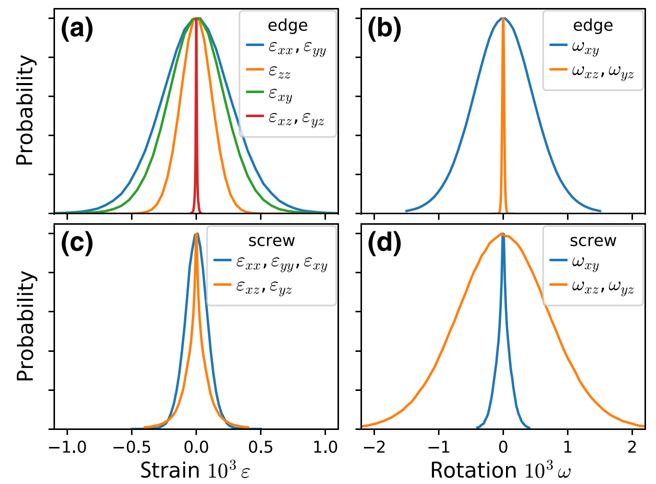


FIG. 14. Probability density distributions of the components of (a),(c) strain and (b),(d) rotation tensors for (a),(b) edge and (c),(d) screw dislocations. Dislocation density $\varrho = 10\ \mu\text{m}^{-2}$ and $M = 8$. Lateral sizes of the free-standing film are $20 \times 20\ \mu\text{m}^2$ film, the strain and rotation components are averaged over a half $l = 150$ nm of the film thickness.

Figure 14 shows the probability density distributions of all components of the strain and rotation tensors for edge and screw dislocations of the same density $\varrho = 10\ \mu\text{m}^{-2}$ and $M = 8$. Figures 14(b) and 14(d) show that the in-plane rotations $\omega_{xy}$ are almost entirely due to edge dislocations, while $\omega_{xz}$, $\omega_{yz}$ are due to screw dislocations. Hence, the analysis of these rotation components can be performed separately to obtain independently the densities of edge and screw dislocations.

Figure 15(a) presents the probability distributions of the strain $\varepsilon_{xx}$ for two arrays of edge dislocations differing in both dislocation densities and the distance of the dislocation pairs. These parameters are intentionally chosen so that the probability distributions practically coincide. The inset in Fig. 15(a) shows the same probability distributions in the log-log scale, thus revealing the asymptotic of the probabilities at large strains. The curves shown in the inset requires substantial statistics and are obtained by repeating the calculation shown in Fig. 13(d) enough times for random arrays of dislocations. In the Stokes-Wilson approximation, these strain probability curves coincide with the intensity profiles measured by an ordinary x-ray diffraction from the whole sample [52,53]. In that case, the measurements provide sufficient dynamic range of intensities to obtain experimental curves similar to the ones presented in the inset in Fig. 15(a). Fits of these curves then allow determination of both parameters, $\varrho$ and $M$ [47]. The probability density obtained in the experiment described in the present paper does not provide sufficient statistics to determine the two parameters of the dislocation ensemble unambiguously. This can, however, be achieved by additionally considering the correlation functions.

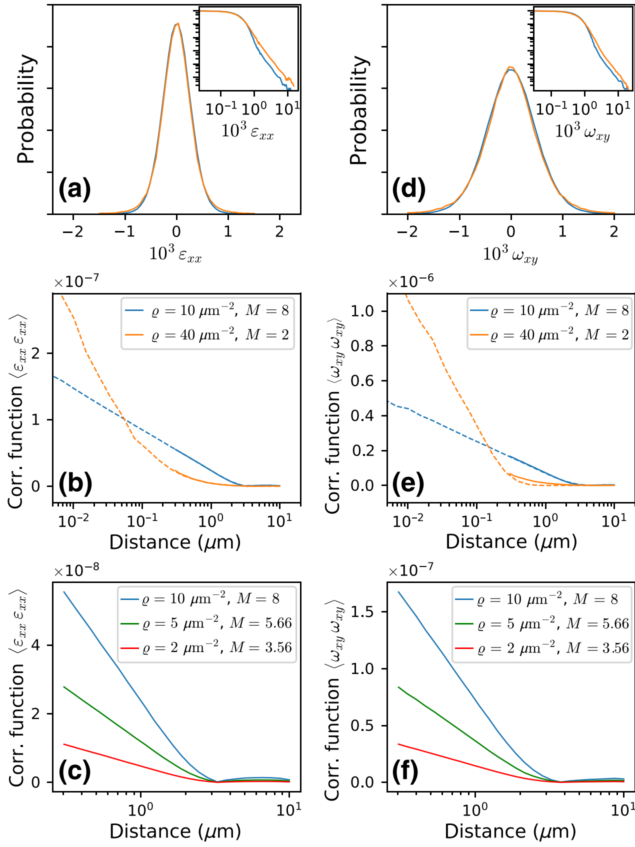


FIG. 15. (a) Probability density distributions of the strain $\varepsilon_{xx}$ for the dislocation arrays of edge dislocations with $\varrho = 10\ \mu\mathrm{m}^{-2}$, $M = 8$ and $\varrho = 40\ \mu\mathrm{m}^{-2}$, $M = 2$ [see legends in (b),(e)]. The inset shows the same distributions in the log-log scale. (b) The autocorrelation functions $\langle\varepsilon_{xx}\varepsilon_{xx}\rangle$ for the same dislocation arrays. The dashed line indicates the part of small distances that is not accessed in our experiment. (c) Autocorrelation functions $\langle\varepsilon_{xx}\varepsilon_{xx}\rangle$ for dislocation arrays with different dislocation densities $\varrho$ and the same radius $R = 2.5\ \mu$m of the screening of the strain fields due to surrounding dislocations. (d) Probability density distributions and (e),(f) autocorrelation functions for the in-plane rotations $\omega_{xy}$ of the same dislocation arrays.

Figure 15(b) presents the autocorrelation functions

$$C(\mathbf{r}) = \left\langle B(\mathbf{r}-\mathbf{r}')B(\mathbf{r}')\right\rangle, \tag{A1}$$

where $B(\mathbf{r})$ denotes any component of strain or rotation produced by the whole dislocation ensemble. The average $\langle\ldots\rangle$ is performed over random positions and orientations of the dislocations. We denote these correlation functions as $\langle B\,B\rangle$ for brevity. Particularly, Fig. 15(b) presents the autocorrelation function $\langle\varepsilon_{xx}\varepsilon_{xx}\rangle$. In our model of the dislocation array as independent pairs of dislocations with opposite Burgers vectors, the total strain or rotation can be written as a sum over dislocation pairs,

$$B(\mathbf{r}) = \sum_j \beta(\mathbf{r}-\mathbf{r}_j), \tag{A2}$$

where $\beta(\mathbf{r})$ is a strain or rotation component due to a dislocation pair. Since the dislocation pairs are independent, the correlation function is

$$C(\mathbf{r}) = \varrho\left\langle \beta(\mathbf{r}-\mathbf{r}')\beta(\mathbf{r}')\right\rangle, \tag{A3}$$

where the average $\langle\ldots\rangle$ is performed over possible Burgers vectors, orientation of a pair, distance between dislocations in a pair, and position $\mathbf{r}'$ of the pair in the plane of the layer. All these averages are performed simultaneously in the Monte Carlo calculation of the correlation functions.

Figure 15(b) presents the autocorrelation function $\langle\varepsilon_{xx}\varepsilon_{xx}\rangle$ for the same dislocation arrays as in Fig. 15(a). As a consequence of the $\varepsilon \propto \rho^{-1}$ dependence of the strain at the dislocation line, the autocorrelation function possesses a $\propto \ln x$ dependence at small $x$, and hence the linear-log scale is used. A notable difference in the correlation functions for two dislocation distributions, that give indistinguishable strain probability distributions in Fig. 15(a), is evident.

The correlation function follows the $\propto \ln x$ dependence as long as the distance $x$ between the correlated points remains smaller than the radius $R$ of the screening of the dislocation strain field by surrounding dislocations. Figure 15(c) compares the autocorrelation functions $\langle\varepsilon_{xx}\varepsilon_{xx}\rangle$ for different dislocation densities $\varrho$ and different values of $M$, chosen so that the screening radius $R = M/\sqrt{\varrho}$ remains the same, $R = 2.5\ \mu$m. The correlation functions possess a linear decrease in the logarithmic scale, with the slope proportional to $\varrho$, as long as $x < R$. At larger separations, the correlations are absent.

Two correlation functions in Fig. 15(b) possess different radii $R$ of the screening of the dislocation strains. The dislocation density $\varrho = 10\ \mu\mathrm{m}^{-2}$ with $M = 8$ gives $R = 2.5\ \mu$m, while $\varrho = 40\ \mu\mathrm{m}^{-2}$ with $M = 2$ gives notably smaller screening radius $R = 0.32\ \mu$m. The minimum distance $x$ presented in the plot is limited by the resolution of the present experiment, and the linear part of the curve is not reached. The dashed lines in Fig. 15(b) extend the calculation of the correlation functions to smaller $x$ and shows that the available range of $x$ may not reveal all features of the curve. Nevertheless, a clear distinction between two curves in Fig. 15(b) shows that the two parameters of the dislocation ensemble, $\varrho$ and $M$, can be unambiguously determined from the correlation functions.

Figures 15(d)–15(f) presents a similar calculation of the probability distributions and the autocorrelation functions of the in-plane rotations $\omega_{xy}$ for the same dislocation arrays. They show that the considerations above are applicable to all components of the strain and rotation tensors of edge and screw dislocations. Finally, combining the results in Figs. 14 and 15, we conclude that the dislocation distribution can be fully characterized by fitting of the autocorrelation functions. Since the rotations $\omega_{xy}$

and $\omega_{xz}$, $\omega_{yz}$ are due to solely edge and screw dislocations, respectively, the autocorrelation functions $\langle\omega_{xy}\omega_{xy}\rangle$ and $\langle\omega_{xz}\omega_{xz}\rangle$ are of primary interest to characterize the dislocation ensemble.

Summarizing, we find that only edge threading dislocations provide the in-plane rotations (twist, $\omega_{xy}$) and the in-plane strain, while screw threading dislocations give rise to the out-of-plane rotations (tilt, $\omega_{xz}$ and $\omega_{yz}$). Hence, edge and screw dislocations (or edge and screw components of mixed dislocations) can be determined separately from the respective probability distributions and autocorrelation functions. The use of only probability distributions does not allow determination of the dislocation density $\varrho$ unambiguously, since the probability distributions depend on two parameters, the density $\varrho$ and the dislocation correlations $M$. Plotting the autocorrelation functions in the linear-log scale, we directly obtain the range of dislocation correlations $R = M/\sqrt{\varrho}$. Hence, a simultaneous fit of the probability distributions and the autocorrelation functions allows to determine the dislocation density unambiguously. The Monte Carlo modeling in the present Appendix is made with the statistics required to obtain smooth curves. However, Fig. 12 above shows that the limited statistics of our experiment is sufficient for quantitative analysis of the dislocation densities and the dislocation correlations.


[1] Y. Sun, S. E. Thompson, and T. Nishida, *Strain Effect in Semiconductors* (Springer, US, 2010).

[2] R. Bierwolf, M. Hohenstein, F. Phillipp, O. Brandt, G. Crook, and K. Ploog, Direct measurement of local lattice distortions in strained layer structures by HREM, Ultramicroscopy **49**, 273 (1993).

[3] T. Schulz, A. Duff, T. Remmele, M. Korytov, T. Markurt, M. Albrecht, L. Lymperakis, J. Neugebauer, C. Chèze, and C. Skierbiszewski, Separating strain from composition in unit cell parameter maps obtained from aberration corrected high resolution transmission electron microscopy imaging, J. Appl. Phys. **115**, 033113 (2014).

[4] J. Wagner, A. Ramakrishnan, H. Obloh, and M. Maier, Effect of strain and associated piezoelectric fields in InGaN/GaN quantum wells probed by resonant Raman scattering, Appl. Phys. Lett. **74**, 3863 (1999).

[5] G. Capellini, G. Kozlowski, Y. Yamamoto, M. Lisker, C. Wenger, G. Niu, P. Zaumseil, B. Tillack, A. Ghrib, M. de Kersauson, M. E. Kurdi, P. Boucaud, and T. Schroeder, Strain analysis in SiN/Ge microstructures obtained via Si-complementary metal oxide semiconductor compatible approach, J. Appl. Phys. **113**, 013513 (2013).

[6] A. Gassenq, S. Tardif, K. Guilloy, G. O. Dias, N. Pauc, I. Duchemin, D. Rouchon, J.-M. Hartmann, J. Widiez, J. Escalante, Y.-M. Niquet, R. Geiger, T. Zabel, H. Sigg, J. Faist, A. Chelnokov, F. Rieutord, V. Reboud, and V. Calvo, Accurate strain measurements in highly strained Ge microbridges, Appl. Phys. Lett. **108**, 241902 (2016).

[7] A. J. Wilkinson and D. Randman, Determination of elastic strain fields and geometrically necessary dislocation distributions near nanoindents using electron back scatter diffraction, Philos. Mag. **90**, 1159 (2010).

[8] A. J. Wilkinson, Assessment of lattice strain, rotation and dislocation content using electron back-scatter diffraction, J. Phys.: Conf. Ser. **326**, 012004 (2011).

[9] G. Naresh-Kumar, B. Hourahine, P. R. Edwards, A. P. Day, A. Winkelmann, A. J. Wilkinson, P. J. Parbrook, G. England, and C. Trager-Cowan, Rapid Nondestructive Analysis of Threading Dislocations in Wurtzite Materials using the Scanning Electron Microscope, Phys. Rev. Lett. **108**, 135503 (2012).

[10] A. Vilalta-Clemente, G. Naresh-Kumar, M. Nouf-Allehiani, P. Gamarra, M. di Forte-Poisson, C. Trager-Cowan, and A. Wilkinson, Cross-correlation based high resolution electron backscatter diffraction and electron channelling contrast imaging for strain mapping and dislocation distributions in InAlN thin films, Acta. Mater. **125**, 125 (2017).

[11] T. U. Schülli and S. J. Leake, X-ray nanobeam diffraction imaging of materials, Current Opin. Solid State Mater. Sci. **22**, 188 (2018).

[12] G. A. Chahine, M.-I. Richard, R. A. Homs-Regojo, T. N. Tran-Caliste, D. Carbone, V. L. R. Jacques, R. Grifone, P. Boesecke, J. Katzer, I. Costina, H. Djazouli, T. Schroeder, and T. U. Schülli, Imaging of strain and lattice orientation by quick scanning x-ray microscopy combined with three-dimensional reciprocal space mapping, J. Appl. Crystallogr. **47**, 762 (2014).

[13] L. Chayanun, S. Hammarberg, H. Dierks, G. Otnes, A. Björling, M. T. Borgström, and J. Wallentin, Combining nanofocused x-rays with electrical measurements at the NanoMAX beamline, Crystals **9**, 432 (2019).

[14] O. Robach, J.-S. Micha, O. Ulrich, O. Geaymond, O. Sicardy, J. Härtwig, and F. Rieutord, A tunable multicolour 'rainbow' filter for improved stress and dislocation density field mapping in polycrystals using x-ray laue microdiffraction, Acta Crystallogr. Sect. A Found. Crystallogr. **69**, 164 (2013).

[15] S. Tardif, A. Gassenq, K. Guilloy, N. Pauc, G. O. Dias, J.-M. Hartmann, J. Widiez, T. Zabel, E. Marin, H. Sigg, J. Faist, A. Chelnokov, V. Reboud, V. Calvo, J.-S. Micha, O. Robach, and F. Rieutord, Lattice strain and tilt mapping in stressed Ge microstructures using x-ray laue microdiffraction and rainbow filtering, J. Appl. Crystallogr. **49**, 1402 (2016).

[16] M. A. Pfeifer, G. J. Williams, I. A. Vartanyants, R. Harder, and I. K. Robinson, Three-dimensional mapping of a deformation field inside a nanocrystal, Nature **442**, 63 (2006).

[17] F. Hofmann, E. Tarleton, R. J. Harder, N. W. Phillips, P.-W. Ma, J. N. Clark, I. K. Robinson, B. Abbey, W. Liu, and C. E. Beck, 3D lattice distortions and defect structures in ion-implanted nano-crystals, Sci. Rep. **7**, 45993 (2017).

[18] F. Hofmann, N. W. Phillips, S. Das, P. Karamched, G. M. Hughes, J. O. Douglas, W. Cha, and W. Liu, Nanoscale imaging of the full strain tensor of specific dislocations extracted from a bulk sample, Phys. Rev. Mater. **4**, 013801 (2020).

[19] M.-I. Richard, T. W. Cornelius, F. Lauraux, J.-B. Molin, C. Kirchlechner, S. J. Leake, J. Carnis, T. U. Schülli, L.

Thilly, and O. Thomas, Variable-wavelength quick scanning nanofocused x-ray microscopy for in situ strain and tilt mapping, Small **16**, 1905990 (2020).

[20] M. H. Zoellner, M.-I. Richard, G. A. Chahine, P. Zaumseil, C. Reich, G. Capellini, F. Montalenti, A. Marzegalli, Y.-H. Xie, T. U. Schülli, M. Häberlen, P. Storck, and T. Schroeder, Imaging structure and composition homogeneity of 300 mm SiGe virtual substrates for advanced CMOS applications by scanning x-ray diffraction microscopy, ACS Appl. Mater. Interfaces **7**, 9031 (2015).

[21] M. H. Zoellner, G. A. Chahine, L. Lahourcade, C. Mounir, C. L. Manganelli, T. U. Schülli, U. T. Schwarz, R. Zeisel, and T. Schroeder, Correlation of optical, structural, and compositional properties with V-pit distribution in InGaN/GaN multiquantum wells, ACS Appl. Mater. Interfaces **11**, 22834 (2019).

[22] Z. Mi and C. Jagadish, *III-Nitride Semiconductor Optoelectronics, ISSN* (Academic Press, Elsevier, Cambridge, 2017).

[23] B. Gil, ed., *III-Nitride Semiconductors and their Modern Devices* (Oxford University Press, Oxford, 2013).

[24] I. Akasaki and H. Amano, Crystal growth and conductivity control of group III nitride semiconductors and their application to short wavelength light emitters, Jpn. J. Appl. Phys. **36**, 5393 (1997).

[25] S. Nakamura and G. Fasol, *The Blue Laser Diode:* GaN *Based Light Emitters and Lasers* (Springer, Berlin Heidelberg, 2013).

[26] B. J. Baliga, Gallium nitride devices for power electronic applications, Semicond. Sci. Technol. **28**, 074011 (2013).

[27] J. Wu, When group-III nitrides go infrared: New properties and perspectives, J. Appl. Phys. **106**, 011101 (2009).

[28] Y. Narukawa, M. Ichikawa, D. Sanga, M. Sano, and T. Mukai, White light emitting diodes with super-high luminous efficacy, J. Phys. D: Appl. Phys. **43**, 354002 (2010).

[29] S. S. Pasayat, C. Gupta, M. S. Wong, R. Ley, M. J. Gordon, S. P. DenBaars, S. Nakamura, S. Keller, and U. K. Mishra, Demonstration of ultra-small ($< 10\ \mu$m) 632 nm red InGaN micro-LEDs with useful on-wafer external quantum efficiency ($> 0.2\%$) for mini-displays, Appl. Phys. Exp. **14**, 011004 (2020).

[30] L. Lymperakis, T. Schulz, C. Freysoldt, M. Anikeeva, Z. Chen, X. Zheng, B. Shen, C. Chèze, M. Siekacz, X. Q. Wang, M. Albrecht, and J. Neugebauer, Elastically frustrated rehybridization: Origin of chemical order and compositional limits in InGaN quantum wells, Phys. Rev. Mater. **2**, 011601 (2018).

[31] A. Dussaigne, F. Barbier, B. Samuel, A. Even, R. Templier, F. Lévy, O. Ledoux, M. Rozhavskaia, and D. Sotta, Strongly reduced V-pit density on InGaNOS substrate by using InGaN/GaN superlattice, J. Cryst. Growth **533**, 125481 (2020).

[32] A. Even, G. Laval, O. Ledoux, P. Ferret, D. Sotta, E. Guiot, F. Levy, I. C. Robin, and A. Dussaigne, Enhanced in incorporation in full InGaN heterostructure grown on relaxed InGaN pseudo-substrate, Appl. Phys. Lett. **110**, 262103 (2017).

[33] A. Dussaigne, F. Barbier, B. Damilano, S. Chenot, A. Grenier, A. M. Papon, B. Samuel, B. B. Bakir, D. Vaufrey, J. C. Pillet, A. Gasse, O. Ledoux, M. Rozhavskaya, and D. Sotta, Full InGaN red light emitting diodes, J. Appl. Phys. **128**, 135704 (2020).

[34] A. Tauzin, T. Akatsu, M. Rabarot, J. Dechamp, M. Zussy, H. Moriceau, J. Michaud, A. Charvet, L. D. Cioccio, F. Fournel, J. Garrione, B. Faure, F. Letertre, and N. Kernevez, Transfers of 2-inch GaN films onto sapphire substrates using smart Cut$^{TM}$ technology, Electron. Lett. **41**, 668 (2005).

[35] C. Ponchut, J. Clément, J.-M. Rigal, E. Papillon, J. Vallerga, D. LaMarra, and B. Mikulec, Photon-counting x-ray imaging at kilohertz frame rates, Nucl. Instrum. Methods Phys. Res. Sect. A: Accelerators, Spectrometers, Detectors and Associated Equipment **576**, 109 (2007).

[36] See the Supplemental Material at http://link.aps.org/supplemental/10.1103/PhysRevApplied.18.064015, which includes Refs. [54–56]. It also includes the derivation of strain and rotation fields of threading dislocations in the thin crystal slab, plots of the correlation functions of the data and further details on the data analysis.

[37] M. Lohmeier and E. Vlieg, Angle calculations for a six-circle surface x-ray diffractometer, J. Appl. Crystallogr. **26**, 706 (1993).

[38] D. Eberly, Euler angle formulas, Geometric Tools, LLC, Technical Report, 1 (2008).

[39] M.-Y. Xie, F. Tasnádi, I. A. Abrikosov, L. Hultman, and V. Darakchieva, Elastic constants, composition, and piezoelectric polarization in $In_xAl_{1-x}N$: From ab initio calculations to experimental implications for the applicability of Vegard's rule, Phys. Rev. B **86**, 155310 (2012).

[40] M. A. Moram and M. E. Vickers, X-ray diffraction of III-nitrides, Rep. Prog. Phys. **72**, 036502 (2009).

[41] R. Butté, L. Lahourcade, T. K. Uždavinys, G. Callsen, M. Mensi, M. Glauser, G. Rossbach, D. Martin, J.-F. Carlin, S. Marcinkevičius, and N. Grandjean, Optical absorption edge broadening in thick InGaN layers: Random alloy atomic disorder and growth mode induced fluctuations, Appl. Phys. Lett. **112**, 032106 (2018).

[42] P. Anderson, J. Hirth, and J. Lothe, *Theory of Dislocations* (Cambridge University Press, New York, 2017).

[43] A. M. Kosevich, in *Dislocations in Solids*, Vol. 1, edited by F. R. N. Nabarro (North Holland, Amsterdam, 1979) Chap. 1.

[44] T. Metzger, R. Höpler, E. Born, O. Ambacher, M. Stutzmann, R. Stömmer, M. Schuster, H. Göbel, S. Christiansen, M. Albrecht, and H. P. Strunk, Defect structure of epitaxial GaN films determined by transmission electron microscopy and triple-axis x-ray diffractometry, Philos. Mag. A **77**, 1013 (1998).

[45] E. Melan and H. Parkus, *Wärmespannungen infolge stationärer Temperaturfelder* (Springer, Wien, 1953) Chap. V.

[46] A. Polian, M. Grimsditch, and I. Grzegory, Elastic constants of gallium nitride, J. Appl. Phys. **79**, 3343 (1996).

[47] V. M. Kaganer, O. Brandt, A. Trampert, and K. H. Ploog, X-ray diffraction peak profiles from threading dislocations in GaN epitaxial films, Phys. Rev. B **72**, 045423 (2005).

[48] V. M. Kaganer and K. K. Sabelfeld, X-ray diffraction peaks from correlated dislocations: Monte carlo study of dislocation screening, Acta Cryst. A **66**, 703 (2010).
[49] M. Wilkens, The determination of density distribution of dislocations in deformed single crystals from broadened x-ray diffraction profiles, Phys. Stat. Sol. (a) **2**, 359 (1970).
[50] M. Wilkens, in *Fundamental Aspects of Dislocation Theory*, edited by J. A. Simmons, R. de Wit, and R. Bullough (Nat. Bur. Stand. (U.S.) Spec. Publ., Washington, D.C., 1970), p. 1195.
[51] M. Wilkens, Broadening of x-ray diffraction lines of crystals containing dislocation distributions, Kristall und Technik. **11**, 1159 (1976).
[52] A. R. Stokes and A. J. C. Wilson, The diffraction of x rays by distorted crystal aggregates — I, Proc. Phys. Soc. London **56**, 174 (1944).
[53] V. M. Kaganer and K. K. Sabelfeld, Strain distributions and diffraction peak profiles from crystals with dislocations, Acta Cryst. A **70**, 457 (2014).
[54] W. S. Slaughter, *The Linearized Theory of Elasticity* (Springer, N.Y., 2002).
[55] J. D. Eshelby and A. N. Stroh, Dislocations in thin plates, Philos. Mag. **42**, 1401 (1951).
[56] A. Yu. Belov, in *Elastic Strain Fields and Dislocation Mobility*, edited by V. L. Indenbom and J. Lothe (North-Holland, Amsterdam, 1992) Chap. 6.